energies

MDPI

Article

Advanced Insulation Materials for Facades: Analyzing Detachments Using Numerical Simulations and Infrared Thermography

Stefano Perilli [1], Davide Palumbo [2], Stefano Sfarra [3,*] and Umberto Galietti [2]

[1] Independent Researcher, Santa Rufina di Roio, 67100 L'Aquila, Italy; stefanoperilli.ps@gmail.com
[2] Department of Mechanics Mathematics and Management (DMMM), Politecnico di Bari, Via Orabona, 4, 70125 Bari, Italy; davide.palumbo@poliba.it (D.P.); umberto.galietti@poliba.it (U.G.)
[3] Department of Industrial and Information Engineering and Economics (DIIIE), University of L'Aquila, 67100 L'Aquila, Italy
* Correspondence: stefano.sfarra@univaq.it; Tel.: +39-340-6151350

Abstract: In building construction, it is very important to reduce energy consumption and provide thermal comfort. In this regard, defects in insulating panels can compromise the capability of these panels of reducing the heat flow by conduction with the surroundings. In recent years, both experimental techniques and numerical methods have been used for investigating the effect of defects on the thermal behavior of building panels. The main novelty of this work regards the application of both numerical and experimental approaches based on infrared thermography techniques for studying the effects of defects such as debonding on the insulation properties of cork panels. In particular, the effects of defects were investigated by using the Long Pulse Thermography technique and then by analyzing the thermal behavior of the panel during the cooling phase. Results show the capability of the proposed approaches in describing the effects of defects in cork panels such as detachments and the benefit effect of a shield coating in improving the insulation properties of the panel.

Keywords: insulating materials; thermography; cork panels; numerical simulations; detachments

Citation: Perilli, S.; Palumbo, D.; Sfarra, S.; Galietti, U. Advanced Insulation Materials for Facades: Analyzing Detachments Using Numerical Simulations and Infrared Thermography. *Energies* **2021**, *14*, 7546. https://doi.org/10.3390/en14227546

Academic Editor: Rodrigo Llopis

Received: 23 September 2021
Accepted: 8 November 2021
Published: 11 November 2021

1. Introduction

Insulating materials are used in building in the residential, commercial, and industrial sectors [1–5] for reducing energy consumption and providing thermal comfort. Malanho et al. [6] described how, due to the growing concern with the environment, systems are being developed with more sustainable and ecological materials, such as ICB (expanded cork). The results showed that the systems with ICB obtained satisfactory global behavior comparable with the EPS systems. The ICB sustainable systems analyzed stood out in acoustic performance. In this regard, insulation techniques allow for retarding the heat flow by conduction with the surroundings in buildings to retain heat/cool within the house [5]. Lagorce-Tachon et al. [7] showed the specific physical properties of alveolar cork structures, such as low permeability to liquids and gases, advanced thermal and acoustic insulation, and high elasticity. Moreover, a morphological analysis of natural cork cells was presented including statistical distributions of structural quantities. Liu et al. [8] prepared cement–cork mortars with different cork volume admixtures. In particular, the fresh state consistency and compressive strength of cement–cork mortars were studied. The porosity and pore distribution characteristics of the prepared samples were obtained using microparticle mercury porosimeter. Merabti et al. [9] proposed the study of mechanical and thermal properties of cement composites with waste cork under different curing conditions. The effect of including granulated blast furnace slag on these composites was also studied.

Insulating materials can be classified both according to heat exchange properties and to their composition [5]. It is common in civil structures to protect the insulation

panels with thin juxtaposed layers. Generally, these thin layers protect the insulation from atmospheric agents and make it more aesthetically pleasing. In this specific case, the thin layer contributes to the insulating effect.

Among the many insulation panels, cork can be considered a mass organic insulation material. It is composed of a huge number of tiny air trapped pockets that allow for reducing the heat flow rate by conduction [5]. Moreover, thanks to its lightweight nature, when joined to other insulation properties related to electric, sound and vibration behavior, cork represents an excellent material for thermal insulation purposes [4,5]. Novais et al. [10] provided new information on the impact generated by cork particle size on thermal properties.

Insulating materials are commonly coupled with insulated panels by means of adhesives (bonded panels) that allow for obtaining an effective and low-cost solution. Sometimes, the insulating material contains the adhesive in itself for allowing the user a simple (manual or automated) application. However, defects can occur between the two couplants (or beneath them) that can produce a partial detachment of the insulating material that can affect the correct behavior of the insulated panels. In this regard, Non-Destructive Techniques (NDT) represent a useful tool for evaluating detachments in insulated panels as they can detect hidden defects without causing damage [11–16].

Stimulated Thermography techniques (ST), with respect to other traditional well established NDT techniques, potentially allow for investigation of large areas with a relatively shorter time and without the need for couplings such as Ultrasonic Testing (UT) or safety issues such as with X-ray, which makes it particularly suitable for the inspection of large structures [17–19]. The most diffused thermographic techniques for the non-destructive evaluation of composite materials are Lock-in Thermography (LT), Pulsed (PT) and Stepped Heating/Long Pulse Thermography (SH/LP) [17–19]. All of these techniques need a heat source to stimulate the material and equipment to analyze the temperature behavior on the surface of the component. The main idea is that a defect inducing different thermophysical local properties in the material will also induce an anomaly in the thermal diffusion, and then a different surface temperature of the component [17–19].

In the last several years, ST has been used for investigating building structures/components principally for obtaining information regarding both the thermal behavior and the structural integrity [14–19]. In the work of Meola [14], the attention was focused on the non-destructive evaluation of masonry structures by means of ST. Different defects have been simulated within one-layer and two-layer specimens and the capability of the thermography in detecting the different nature of each defect has been demonstrated.

Regarding the cork used in building, in the literature, there are many works in which the thermal properties have been evaluated by using numerical and experimental methods [20–24]. In the work of Perilli et al. [20], a numerical approach based on experimental data was adopted for exploring the insulation properties of cork panels. In particular, the benefit of using a shield coating for minimizing the subsurface detachment was demonstrated by means of a numerical model developed in Comsol®. The cork–coconut–cork panel with a Phase Change Material (PCM) was investigated in the work of Sfarra et al. [21]. Moreover, the thermophysical effect of a fabricated subsurface defect has been investigated with and without the PCM.

Although several studies have been presented on cork panels, none of them involved a full field experimental technique such as the thermography technique for validating the numerical model and evaluating the capability of detection of defects such as detachments. In this regard, the main novelty of this work was to investigate the effects of defects such as debonding on the insulation properties of cork panels by means of a novel approach based on simulations and experimental thermographic tests. In particular, the analysis was focused on the thermal behavior of a cork panel coated with an insulating protective material (COIB 250®) and with a fabricated detachment, subjected to a Long Pulse test.

The results show the capability of the Long Pulse technique in detecting detachment in insulating cork panels and the benefits obtained by using a shield coating material.

2. Theory: Long Pulse Thermography

Step Heating/Long Pulse Thermography (SH or ST/LP) [17–19] consists of the application of an input pulse that has longer durations than Pulsed Thermography (PT) to allow the input thermal excitation to reach deeper defects. Unlike PT, in SH/LP the defects are warmer/colder than the surroundings and exchange heat with different rates than non-defective regions. It produces higher discrimination in defect detection.

The feasibility of SH for the detection and characterization of flat bottom holes and buried defects is analytically proven by Badghaish and Fleming, and Balageas and Roche in [25,26], respectively. Specifically, following the developments in [27], the surface temperature of finite thickness structures is initially comparable to the one of semi-infinite structures in the early period but then deviates once the heat pulse reaches the back surface. The specific time instant when the heatwave deviates from Newton's law [28] determines the thickness of the specimen. This value depends on the first integral of the error function, and thus can easily be determined by means of well-known equations [29]. This is important to underline, as these equations are valid only under strict hypotheses and their use can involve significant errors in defect depth and size evaluation.

3. Materials and Methods

3.1. Materials

The object of the investigation is represented by a novel insulation panel constituted of cork and a thin coating of an insulating material to reduce further the thermal conductivity value. The cork layer was obtained firstly shredding the cork in many pieces and then pressing these pieces in order to obtain the desired shape (parallelepiped in this case) [20]. The insulating coating COIB250® with a thickness of 3 mm was deposed on the surface of the panel by means of a suited coating deposition procedure. Firstly, a layer of 0.5 mm was deposed by means of a brush then followed a drying phase of about 30 min just before deposing the remaining layers until reaching the thickness of 3 mm. The final dimensions of the panel were 1000 × 500 × 30 mm.

As already said, these panels are bonded directly on the structure and defects such as detachments can compromise the correct behavior of the insulation. To simulate the detachment, a defect of dimensions 80 × 80 mm was created in the cork panel. In particular, a cubic volume of the cork material was removed from the rear side, taking care to not damage the material close to the cutting zone (Figure 1a). In this way, a groove of cubic shape was obtained. In this regard, a suitable device (Figure 1b) was used for obtaining the desired shape and accuracy. The presence of the air that represents the detached area was simulated by placing a sponge element of dimensions 80 × 80 × 3 mm^3 between the panel and the cubic cork element obtained from the previous working step [30,31]. Figure 1c,d show the necessary steps for the construction of the defect and the cross-section of the panel, respectively. In summary, the defected area was composed of the COIB250® coating, the sponge and the cork element repositioned in the cubic groove.

In Table 1, the thermophysical properties of the materials that compose the panel are reported, where ρ represents the density, k the thermal conductivity and c_p the specific heat capacity of the material. The emissivity values were verified by means of experimental tests according to the Standards ASTM E1862 [31] and ASTM E1933 [32] using tape as a known reference and two halogen lamps for heating the material. The emissivity values found for the cork and the COIB250® were 0.97 and 0.92, respectively. These values are very close to the literature value for the cork and the value provided by the manufacturer for the COIB250®, so, in view of this, we preferred to use the latter for the following analysis.

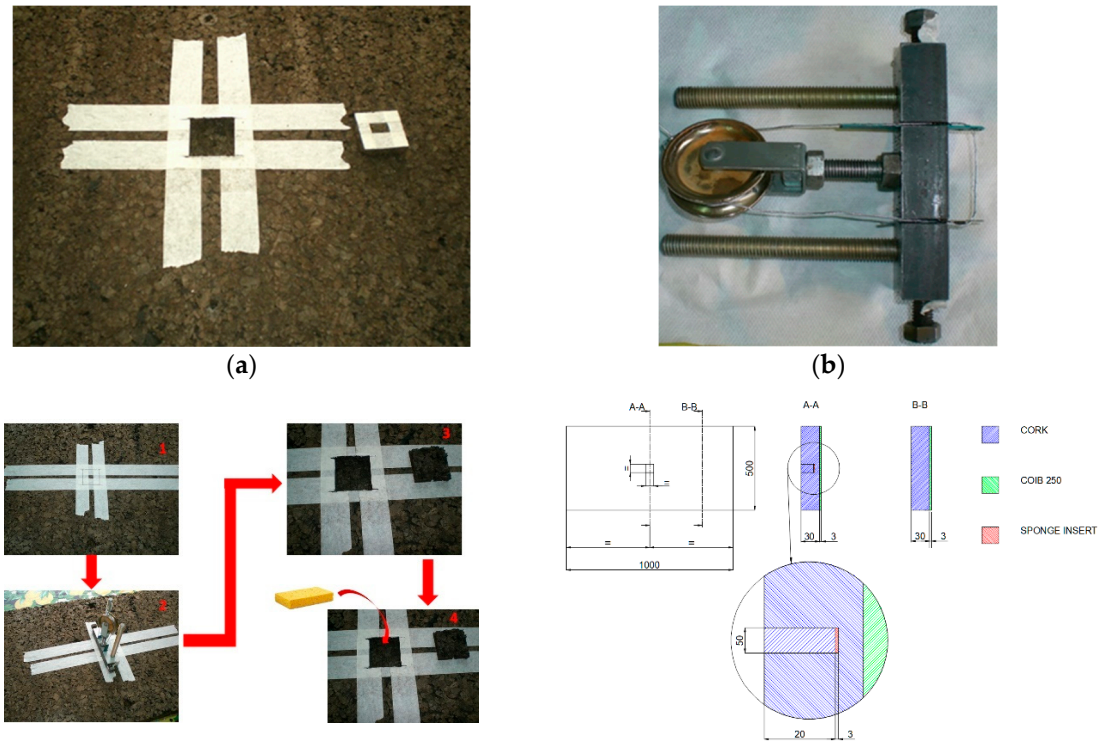

Figure 1. The analyzed panel: (**a**) the flat bottom hole, (**b**) the experimental machine for the execution of the flat bottom hole, (**c**) necessary steps for the construction of the defect, (**d**) the cross-section of the panel.

Table 1. Technical characteristics of the materials.

Materials	Dimensions (mm^3)	ρ (kg/m^3)	k (W/mK)	c_p (kJ/kgK)	Surface Emissivity	Volume Fraction
Cork	1000 × 500 × 30	120 [33]	0.036 [33]	1.9 [33]	0.95 [34]	
Sponge	80 × 80 × 3	0.27(Dry)/0.75(Wet) [35]	0.018 [36]	1.917 [36]		0.67 [36]
COIB250®	1000 × 500 × 3	690 [37]	0.03 [37]	1.93 [38]	0.91	

3.2. Numerical Model (Comsol)

The numerical 3D model was carried out using the Comsol® software importing the geometries of the panel and the heat sources from the CatiaV5® software. In particular, the heat sources (halogen lamps) were modelled as parallelepiped solids placed 1000 mm from the panel in order to simulate the experimental setup (described in the next section). In this regard, and for the same motivation, the panel was placed in contact with a horizontal panel made of wood. Tetrahedral elements were used for meshing all the geometries of the model paying attention to guarantee the continuity rule at the nodes placed at the interface between two different materials. In Figure 2a, the mesh of the whole model is reported, whereas in Figure 2b,c are reported the rear part of the panel placed on the support and a zoomed view of the thickness of the panel, respectively.

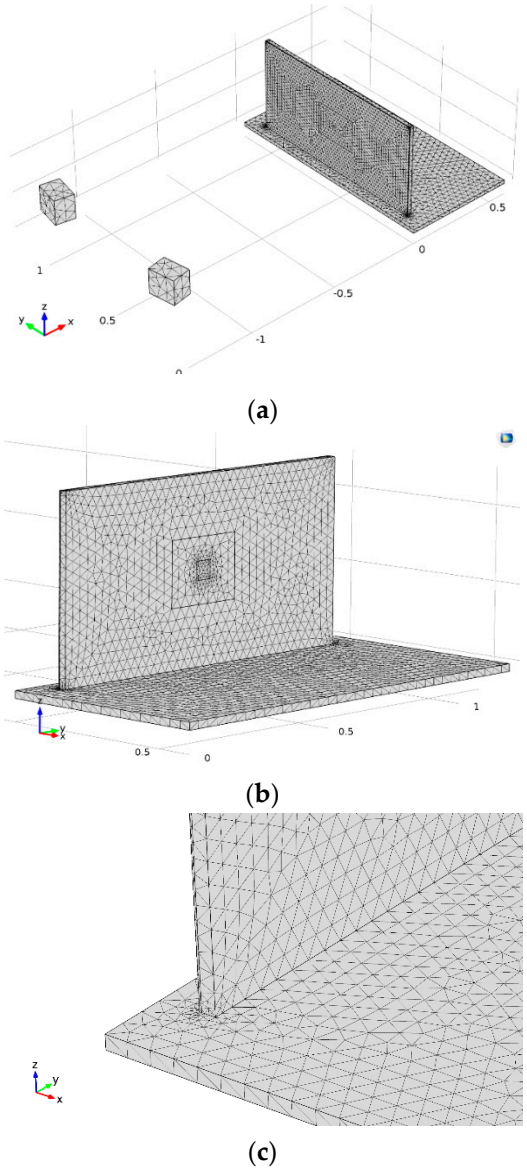

Figure 2. Mesh of the model: (**a**) full model, (**b**) rear view of the cork panel and the support, (**c**) magnification of the contact zone between the cork panel and the support.

In particular, it is important to observe the correspondence of nodal contact among nodal mesh on the panel and nodal mesh on the support. As expected, it was difficult meshing the insulating coating Coib250® due to its thin dimension with respect to the other part of the model (panel and support). Indeed, to obtain the correct mesh capable of describing the heat transmission phenomena between the interface of two materials it was necessary to set the mesh of the two materials to have common nodes at the interface. However, this means increasing the number of elements and then having a dense mesh with a consequent increase in the computational time. In this regard, to reduce the computational cost, for all the parts, except for the insulating Coib250®, the tool "Maximum element growth rate" was used. In this way, the number of nodes as a function of the thickness was effectively reduced. In other words, this tool allows changing the aspect ratio of the tetrahedrons as a function of the thickness. In particular, the "Maximum element growth rate" was increased up to 8% with respect to the nominal value.

In addition, a "free triangular mesh" was used for modelling the heat sources (halogen lamps). In this way, only the surface is considered for the analysis and then the surface temperature of the two heat sources can be obtained. Modelling the two sources as two

separated headlights allowed us to control the superficial temperature and then to verify the imposed excitation power as declared from the manufactured lamps in terms of electrical power. Moreover, in this way, also the thermal inertia of the headlight was considered. Indeed, the headlights heated the sample also during the cooling phase after they were turned off. The simulated lamps were Philips® R7s cap Halogen linear lamp 500 W that reach the bulb temperature of 813.45 K. In Figure 3 the imposed excitation electric power is reported.

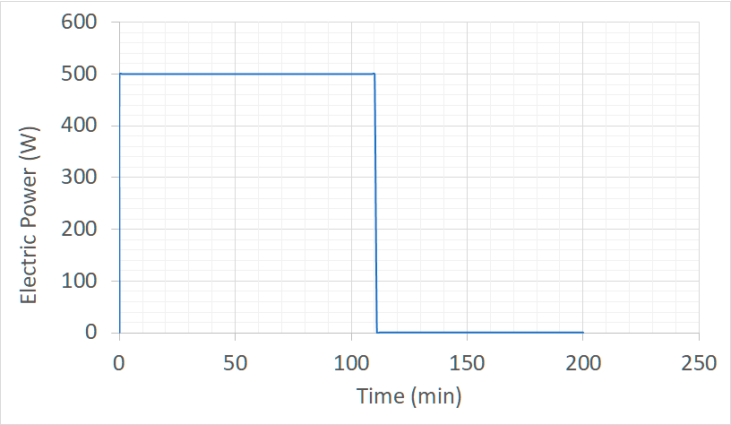

Figure 3. The trend of electrical power versus time of the projectors during the test.

The module used for the analysis was the "Heat Transfer with Radiation in Participating Media" that allows to investigate the behavior of porous panels in the presence of convection, radiation, and conduction [39–41]:

$$\underbrace{\rho C_p\left(\frac{\partial T}{\partial t}+(\boldsymbol{u}\cdot\nabla)T\right)}_{a}=\underbrace{-\nabla\cdot(\boldsymbol{q}_c+\boldsymbol{q}_r)}_{b}+\underbrace{\boldsymbol{\tau}:\boldsymbol{S}}_{c}-\underbrace{\frac{\boldsymbol{T}}{\boldsymbol{\rho}}\frac{\partial\boldsymbol{\rho}}{\partial\boldsymbol{T}}\Big|_{\boldsymbol{p}}\left(\frac{\partial\boldsymbol{p}}{\partial\boldsymbol{t}}+(\boldsymbol{u}\cdot\nabla)p\right)}_{d}+\underbrace{\boldsymbol{Q}}_{e} \quad (1)$$

The first term on the left of Equation (1) (indicated with the letter a) represents the heat power per unit of volume, where: ρ is the density of the fluid (humid air) that surround the material, C_p is the specific heat at constant pressure of the material, T is the temperature and $\boldsymbol{u}$ is the fluid velocity field. For porous materials, the fluid velocity field is considered as the fluid velocity per unit of the cross-section. The mean linear velocity within the porous material is evaluated as uL=u/θL, where θL is the volume porous fraction.

The term b is composed of two parts that represent the heat exchanged for conduction and radiation, respectively. In particular, the conductive term $\boldsymbol{q_c}$ can be written as [40]:

$$\nabla\cdot\left(\boldsymbol{k}_{eff}\nabla T\right) \quad (2)$$

where $\boldsymbol{k_{eff}}$ is the effective conductivity tensor. The radiative term $\boldsymbol{q_r}$ involves all the thermal phenomena related to the radiative heat transfer by means of the Radiative transfer analysis: incident radiation, adsorbed radiation, emitted radiation, transmitted radiation, and scattered radiation. Considering the intensity of the radiation I(Ω) travelling along the direction Ω, the scattered radiation coming from a known direction Ω can be expressed as [42]:

$$\frac{1}{4\pi}\int_{4\pi}\phi(\Omega_i,\Omega_j)d\Omega_i=1 \quad (3)$$

where the phase function $\Phi(\Omega_i, \Omega_j)$ defines the probability that a single ray coming from the direction $\Omega_{i\text{-th}}$ can be scattered in the $\Omega_{j\text{-th}}$ direction. Moreover, the intensity of the radiation

along a given direction can be either attenuated or scattered. In this regard, an additional term σ_s can be considered for the fractions of radiations attenuated or scattered [42]:

$$\frac{\sigma_s}{4\pi}\int_{4\pi}\phi(\Omega_i,\Omega_j)d\Omega_i = 1 \tag{4}$$

The global heat radiation in the heat transfer equation can be expressed by means of the following equation [42]:

$$\Omega\cdot\nabla I(\Omega) = k_e I_b(T) - \beta I(\Omega) + \frac{\sigma_s}{4\pi}\int_0^{4\pi} I(\Omega_i)\phi(\Omega_i,\Omega_j)d\Omega_i \tag{5}$$

where T is the atmospheric temperature, k_a is the coefficient of absorption, $\beta = (k_a + \sigma_s)$ is the extinction coefficient, k_e is the emissivity coefficient and I_b is the radiation of the black body.

The phase function depends also on the material. In this work, this function was modelled as a linear function considering the anisotropic behavior of the material [42]:

$$\phi(\mu_0) = 1 + a_1\mu_0 \tag{6}$$

where μ_0 is the angle between the direction of the scattered radiation and the osculating plane of the surface reached by the radiation, whereas the coefficient a_1 represents the probability of scattering in any direction. In this way, a_1 is equal to 0 for material with isotropic behavior (the scattering probability is the same in any direction) and assumes a negative value for materials with anisotropic behavior.

The term indicated with the symbol c in Equation (1) represents the double dot product between the stress tensor $\boldsymbol{\tau}$ and the strain tensor $\boldsymbol{S}$, this latter is expressed as [39,40]:

$$\boldsymbol{S} = \frac{1}{2}\left(\nabla\boldsymbol{u} + \nabla\boldsymbol{u}^T\right) \tag{7}$$

The term d is composed of two sub–terms indicated with the numbers 1 and 2 in Equation (8) [39,40]:

$$\underbrace{\frac{\boldsymbol{T}}{\boldsymbol{\rho}}\frac{\partial\boldsymbol{\rho}}{\partial\boldsymbol{T}}\bigg|_{\boldsymbol{p}}}_{1}\underbrace{\left(\frac{\partial\boldsymbol{p}}{\partial\boldsymbol{t}} + (\boldsymbol{u}\cdot\nabla)p\right)}_{2} \tag{8}$$

where the first term considers the variation of the air density as a function of the temperature, at constant pressure, whereas the term 2 represents the mass conservation law referring to the air surrounding both the specimen and the headlights. Finally, the term e refers to heat sources characterized by energy dissipation phenomena.

3.3. Experimental Tests

To validate the numerical results an experimental Long Pulse test was carried out as reported in Table 2. The experimental setup is reported in Figure 4, in which two halogen lamps of power of 500 W, placed at a distance of 1.20 m, were used for exciting the component and the IR camera FLIR 655sc with a 640 × 480 microbolometer detector used for acquiring the thermal sequence. The two lamps were controlled by the MultiDES® system.

Table 2. Main information regarding the experimental tests.

Step Heating Duration (min)	Cooling Phase Duration (min)	Frame Rate (Hz)
110	90	0.05

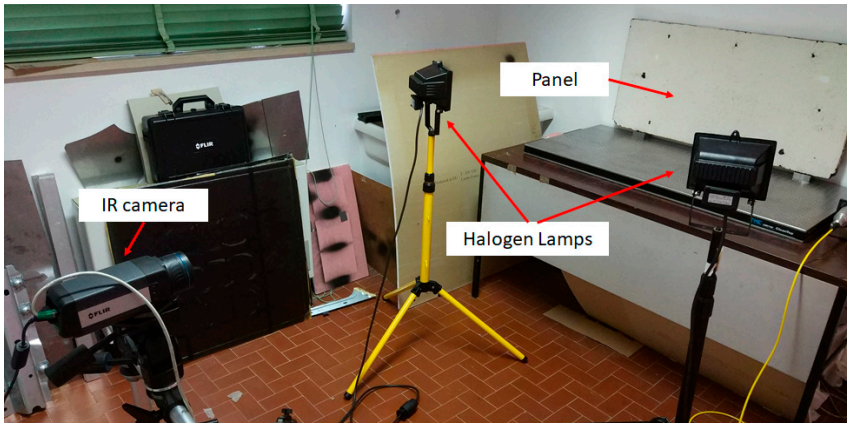

Figure 4. View of the experimental setup (thermographic test) used for performing the LP test: IR camera (model Flir A655sc), halogen lamps (500 Wx2) and the investigated panel.

3.4. Data Processing

The thermal sequence was processed by using the software IRTA2® and Matlab®. In particular, the adopted algorithms were the *slope* and R^2 [43] and the Thermal Signal Reconstruction (TSR)® [44], applied only to the cooling phase (Long Pulse analysis).

In TSR, the cooling curve can be fitted in the logarithmic domain by means of a polynomial function (Equation (9)). It has been found that a 5th (or 7th) order polynomial provides an excellent fit to PT data since the inclusion of higher orders terms only replicates noise. As a result, the TSR method provides a significant degree of data compression; in fact, there is a replacement of the sequence of temperature maps in the time, by a series of $(n + 1)$ images that correspond to the polynomial coefficients. From this series of $(n + 1)$ maps, it is possible to reconstruct a full thermographic sequence obtaining, in addition, a drastic reduction of the data amount. It is also convenient to analyses the 1st and the 2nd logarithmic derivatives of the thermographic sequence, which derive directly from the polynomial [44]. For each pixel, the time sequence can be differentiated using these expressions:

$$\ln(\Delta T) = a_0 + a_1 \ln(t) + a_2[\ln(t)]^2 + \ldots + a_n[\ln(t)]^n \quad (9)$$

$$\frac{d\ \ln(\Delta T)}{d\ \ln(t)} = \sum_{n=0}^{N} n a_n [\ln(t)]^{n-1} \quad (10)$$

$$\frac{d^2\ \ln(\Delta T)}{d\ [\ln(t)]^2} = \sum_{n=0}^{N} n a_n [\ln(t)]^{n-2} \quad (11)$$

where a_n are the coefficients of the polynomial function.

The *slope* and R^2 [43] are well-known algorithms based again on the study of the cooling behavior. In fact, the presence of the defect determines a modification of the thermal profile during cooling with a typical non-linear behavior. In the case of a simple linear regression, R^2 equals the square of the Pearson correlation coefficient between the observed and predicted data values of the dependent variable [43].

In Figure 5 is shown, in a schematic way, the adopted procedure for analyzing the thermographic data. The thermal sequence was acquired by means of the IR Max software (by FLIR) and then only the cooling behavior was extracted in terms of a 3D data matrix. Then, the Matlab® software was used for performing the TSR algorithm, whilst the IRTA® software was used for *slope* and R^2 algorithm. The *slope* (m) and R^2 algorithms directly provide two single maps of the two indexes, while the TSR provides the sequences related to the first and second derivative of the polynomial fitting, and then single maps can be extracted.

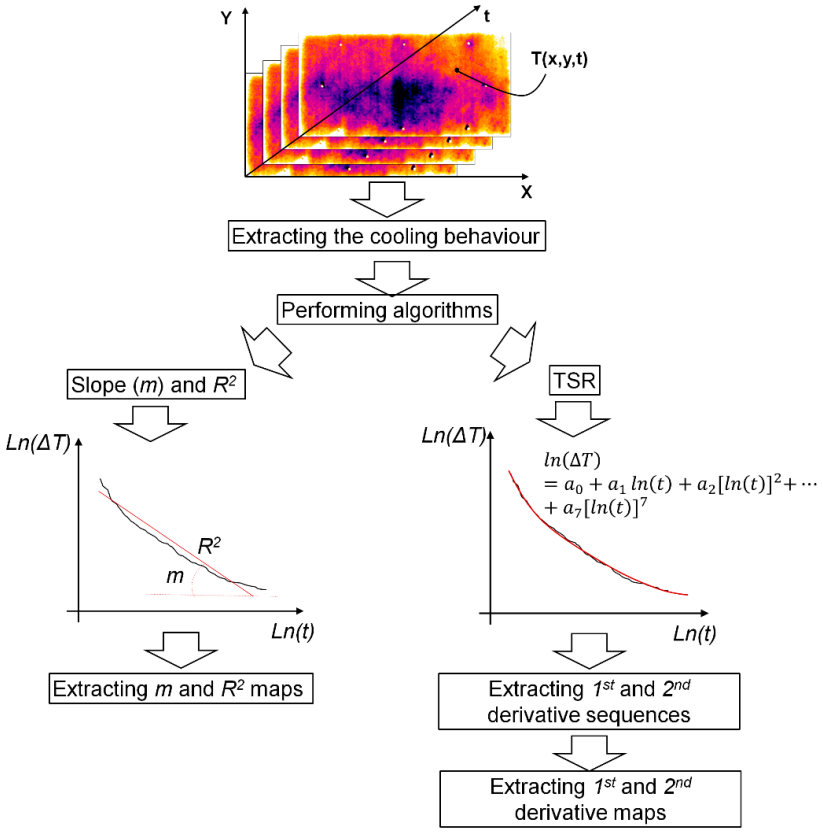

Figure 5. Schematic representation of the data processing procedure.

4. Results and Discussion

4.1. Numerical Model

The results of the numerical model were obtained by setting the Time dependent and Fully Coupled (Pardiso) analysis. In Figure 6, the result in correspondence of the first instant of the analysis is shown.

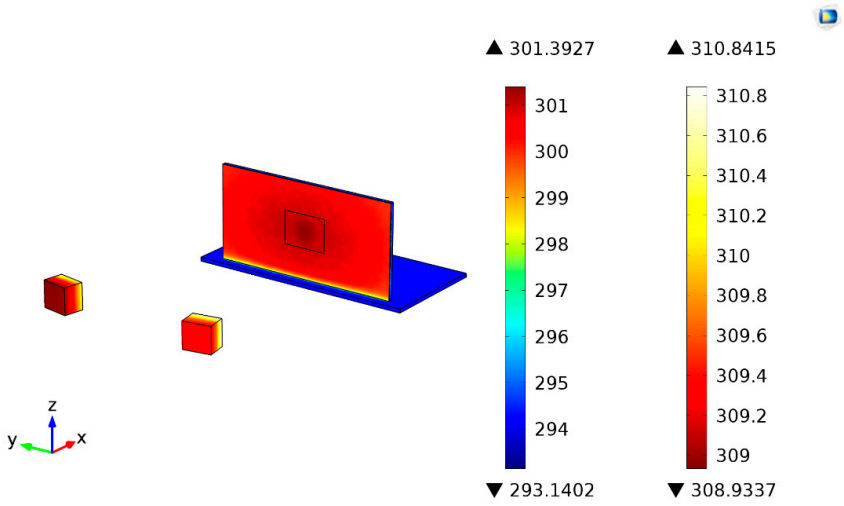

Figure 6. View of the numerical model including the projectors for the first second of analysis. The palette on the left shows the temperature trend of the panel and the support, while the one on the right shows the temperature trend of the projectors.

All the bodies in Figure 6 show the trend of the temperature range for the first second of analysis. The projectors have a very different temperature trend (shown in the right palette) compared to the temperature of the panel and support (shown in the left palette). For just one second of analysis, there is a difference of about 10 K between the projectors and the panel. During both the heating and cooling phases, the lamps assumed temperature values of a higher order than the panel temperature. In this regard, it was very difficult to represent both the panel and lamps with a single scale palette. Therefore, to allow the reader to observe in good detail the distribution of the temperatures on the panel, we preferred to show all the results setting the scale palette, only considering the panel.

In Figure 7, the temperature evolution for different temporal times during the heating excitation is reported. In Figure 7a, the result after 10 min of heating is reported. In particular, the temperature field appears uniformly distributed on the superficial part of the panel with a slightly high value of the temperature in the central part of the specimen with respect to the edges subjected to the well-known edge effects. Small differences in temperature can be observed also in correspondence to the contact zone between the panel and the support. Along the depth direction, temperature variations can be observed only for depth less than 1/4 of the total thickness. In this regard, similar behavior was obtained after 20 min, 30 min, not shown in the figure, and 40 min of heating Figure 7b, with an expected increase of the superficial mean temperature. This characteristic behavior is due to the good insulating properties of the materials composing the panel.

A significant temperature increase along the depth of the panel can be observed after 50 min of heating (Figure 7c) with the rear surface of the panel that is still at the environmental temperature. The maximum temperature is reached after 100 min of heating (Figure 7d) at the center of the frontal surface of the panel (~318 K) with an in-depth thermal diffusion that interested about one-half of the thickness. No significant temperature variations were registered until the end of the heating phase (110 min) (Figure 7e) in which occurs the shutdown of the projectors that involves either a more uniform temperature distribution or a rapid decrease of the temperature (about 0.8 K).

In Figure 7f,g is depicted the temperature distribution during the cooling phase, 10 min and 20 min after the projectors turned off, respectively. In particular, as already said, in this first part of the cooling and then just after the headlights turned off, the temperature tends to drop quickly toward the environment temperature (about 305 K) in all the panel except in the central part in which the defect is placed (about 317 K). Then, the cooling phase was characterized by a uniform temperature decrease until the lower temperature mean value of 299.18 K was observed after 90 min (Figure 7h). During the cooling phase, the mean value of the temperature dropped by ~7 K and this temperature variation involved about 1/3 of the total thickness of the panel.

4.2. Discussion and Experimental Validation

To investigate both the thermal behavior of the panel and the simulated defect over time, four areas were considered, two on the frontal part and two in the rear part of the panel, as indicated in Figure 8. In particular, the chosen areas are representative of the non-defective material and the defected area.

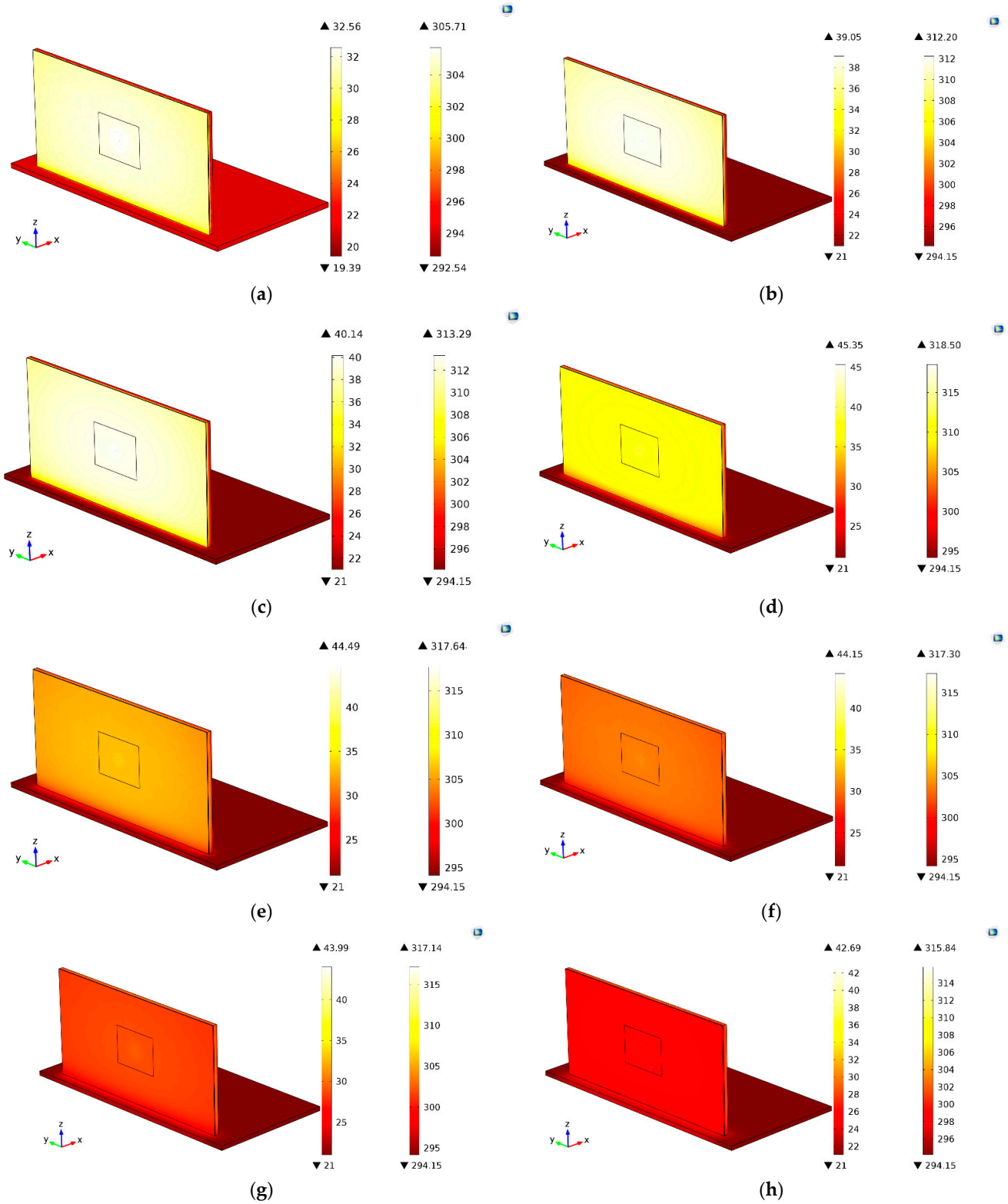

Figure 7. The trend of the temperature field of the model (cork panel and support), at (**a**) 10 min, (**b**) 40 min, (**c**) 50 min, (**d**) 100 min, (**e**) 110 min, (**f**) 120 min, (**g**) 130 min, (**h**) 200 min.

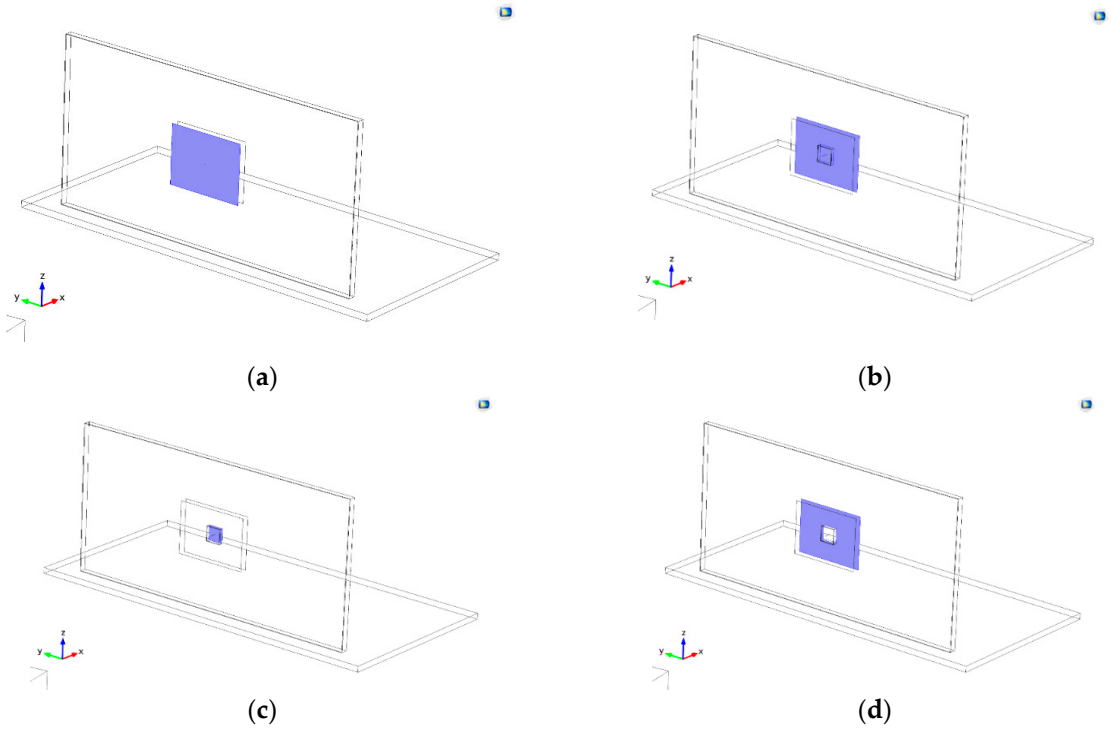

Figure 8. Area of analysis: (**a**) front side, (**b**) rear side, (**c**) rear side including the defect, (**d**) rear side excluding the defect.

In Figure 9, the mean temperature trend of the chosen four areas (ROIs) is reported. Considering the frontal ROIs, the different thermal behavior between the non-defective material and defect can already be seen during the heating phase, just after 10 min after the headlights turn on. However, a better thermal contrast is obtained in correspondence with the maximum temperature value and during the cooling phase. In any case, the defected area always presents a higher temperature value than the non-defective material. The effect of the defect is more evident in the rear part of the panel in which both the maximum temperature and the time in which the maximum temperature is reached are very different with respect to the non-defective material. In particular, the phase shift measured in correspondence of the imposed defect (about 40 min) can be used as an index for evaluating the effect of defects on the insulating properties of the panel (reduction of the phase shift).

In Figure 10, the experimental results, in terms of surface temperature trends (mean values) of the defective and non-defective, areas are reported. The area delimitated by the red dotted line represents the defect nominal area, whereas the non-defective is considered as the area enclosed between the white and red dotted line (Figure 10). Figure 10 shows that there is a good agreement between numerical and experimental results in terms of the temperature trend over time. However, a difference of about 7 K between the approaches was obtained in correspondence to the maximum temperature, but this difference can be considered acceptable for the model validation. At this point, it is important to underline that the numerical model allows for describing the thermal behavior of both the panel and the defect.

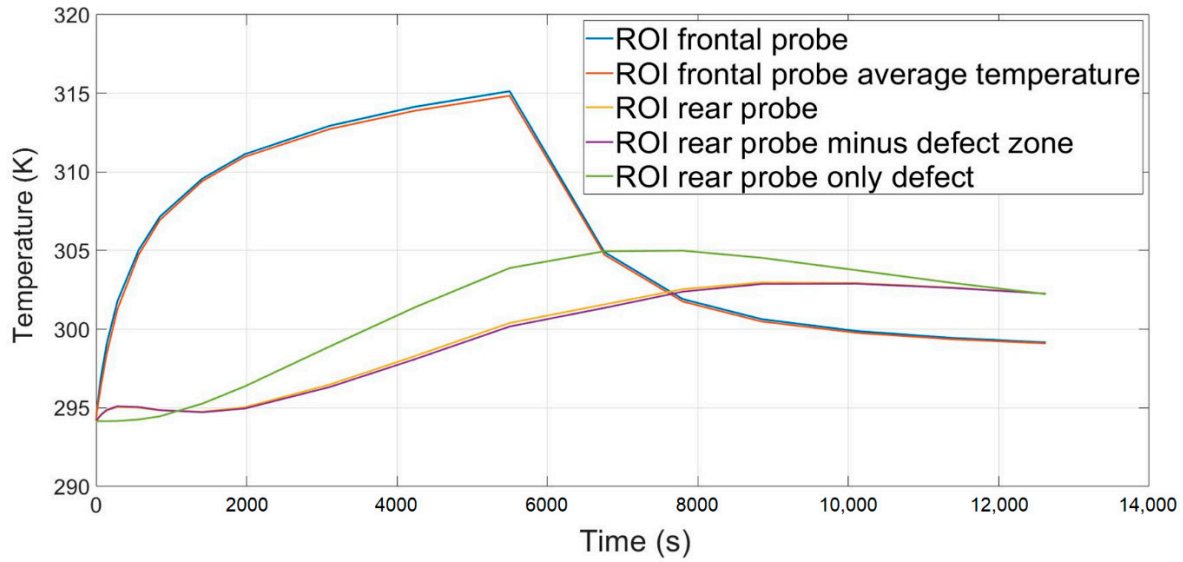

Figure 9. The trend of the temperature over time, evaluated with respect to the virtual probes (Comsol® results).

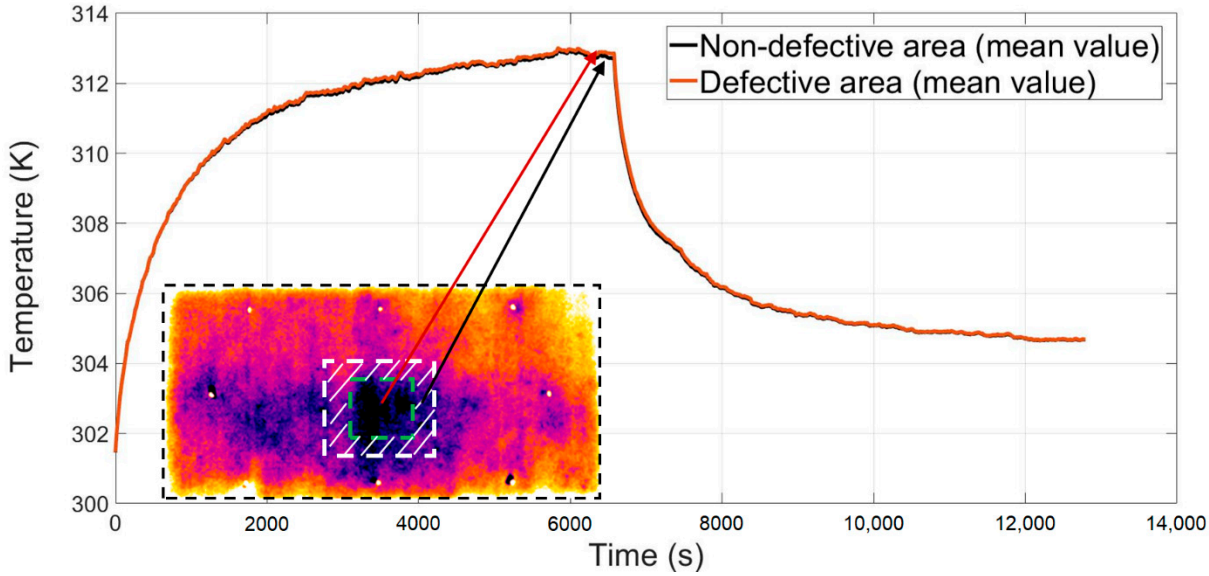

Figure 10. The trend of the temperature over time both for the non-defective (the white area around the defect) and the defective areas (mean values in the green area), (experimental results).

In Figures 11 and 12 the experimental results obtained from the adopted algorithms are reported. It can be seen that only the *slope* data allow for detecting the defect, though with a low signal contrast. Moreover, variation of the *slope* signal can be observed in the whole panel and above all in the non-defective areas in the proximity of the defect. These signal variations can be attributed to the intrinsic properties of the material that is characterized by high porosity and a high level of inhomogeneity. Moreover, a wider area around the defect seems to be involved by a *slope* variation. This can be explained by the presence of detached zones in the proximity of the defect borders.

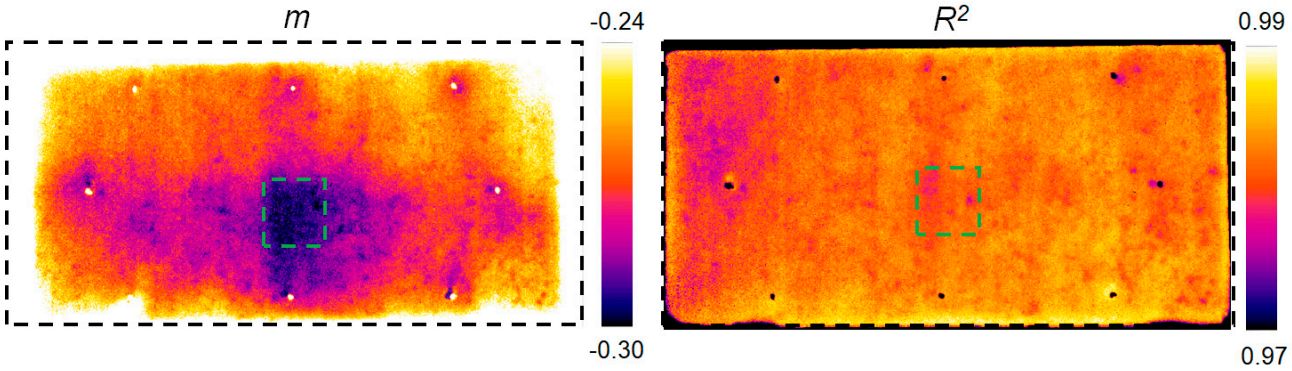

(**a**) (**b**)

Figure 11. The experimental results obtained with the adopted algorithms: (**a**) the *slope* and (**b**) R^2 (the green area represents the defect).

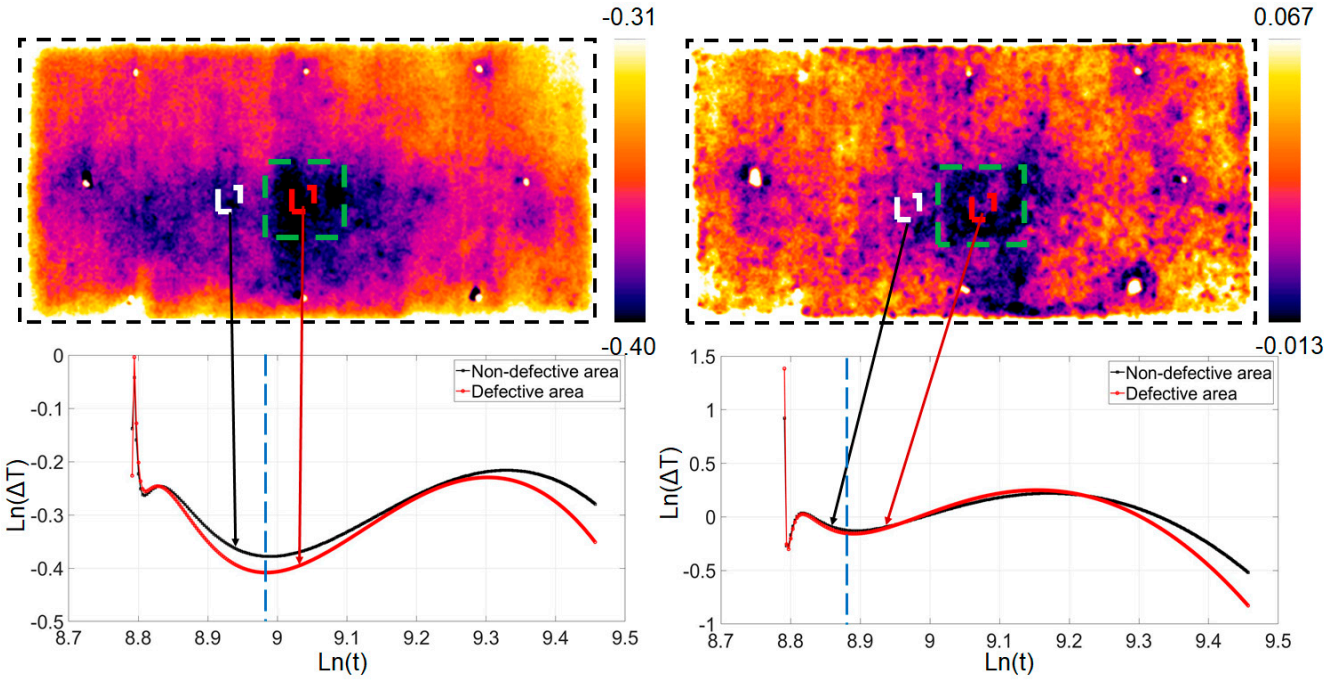

(**a**) (**b**)

Figure 12. The results of the first (**a**) and the second (**b**) derivative of the thermal signal both for the non-defective and the defective area (TSR algorithm). The blue dotted lines represent the times for which the first derivative and the second derivative maps were extracted.

Similar considerations can be performed for the TSR® algorithms. The fitting in the double logarithmic scale of the thermal signal over time was carried out considering a polynomial degree of the 7th order. In Figure 12, the results of the first and second derivative of the thermal signal both for the non-defective and defect is shown. The thermal trends refer to the mean signal evaluated in the area indicated with the dotted white (non-defective) and red (defect) lines. The maps in Figure 12 were extracted in correspondence with the times indicated with the blue dotted lines. Both the first and the second derivative analysis allow to detect the defect but, also, in this case, significant signal variations can be observed on the surface of the panel due to the inhomogeneity of the material.

5. Conclusions

In this work, numerical and experimental tests were carried out for investigating the thermal behavior of an insulating cork panel in the presence of a shield coating and a fabricated defect.

Usually, the insulating material or the layers of insulating materials, are applied on the wall/male masonry. Generally, the thin layers, juxtaposed to the insulating panels, do not actively contribute to the insulation but they protect the insulation materials from atmospheric agents and make them more pleasing aesthetically. In this case, however, the thin layer also contributes to the insulating effect by reducing the transmittance of the whole product and increasing the phase shift. This potentially makes it an advanced insulation material.

A numerical model was developed in Comsol® considering the porous properties of the material and simulating detachment between the cork panel and the shield coating (i.e., the insulating material). Experimental tests with the LP technique were carried out for validating the numerical data and for evaluating the capability of detecting the imposed defect. The main results can be summarized as follows:

1. The numerical model allows for investigating the thermal behavior of insulating cork panels in the presence of a defect. The obtained results are in good agreement with the experimental analysis and could be used for investigating different geometries and configurations of building structures.
2. The Long Pulse Thermography and more specifically the TSR® and *slope* algorithms allow for detecting the imposed defect with a Long Pulse duration of about 110 min and a cooling time of 90 min. However, it is important to underline that the porous nature of the cork can affect the LP results and makes it difficult to detect small and deeper defects.

The obtained results demonstrate the efficiency and effectiveness of the adopted approach for evaluating defects in insulating panels. In this regard, the proposed approach allows for performing a non-destructive analysis and evaluating the defect dimensions. In these terms, it can be used for predicting the thermal behavior of panels in the presence of defects.

Future works will be focused on investigating other configurations and geometries, assessing the sensitivity of detecting the LP technique, as well as using additional non-destructive testing techniques for comparative purposes [45,46].

Author Contributions: Conceptualization, S.P., U.G., S.S. and D.P.; methodology, S.P., U.G., S.S. and D.P.; software, S.P., U.G., S.S. and D.P.; validation, S.P., U.G., S.S. and D.P.; formal analysis, S.P. and D.P.; investigation, S.P., U.G., S.S. and D.P.; resources, S.P., U.G., S.S. and D.P.; data curation, S.P., U.G., S.S. and D.P.; writing—original draft preparation, S.P. and D.P.; writing—review and editing, S.P., U.G., S.S. and D.P.; visualization, S.P., U.G., S.S. and D.P.; supervision, U.G. and S.S.; project administration, S.P., U.G., S.S. and D.P.; funding acquisition, U.G. and S.S.. All authors have read and agreed to the published version of the manuscript.

Funding: This research received no external funding.

Data Availability Statement: Data are available upon reasonable request.

Acknowledgments: The authors would like to thank Mirco Guerrini (Caldo Continuo Srl) for providing the materials inspected/analyzed.

Conflicts of Interest: The authors declare no conflict of interest.

Nomenclature

ρ	Density	kg/m^3
k	Thermal conductivity	W/mK
c_p	Specific heat at constant pressure	kJ/kgK
ε	Surface emissivity	(0–1)
T	Temperature	K
$\boldsymbol{u}$	Fluid velocity field	m/s
θ	Porous fraction	(0–1)
$\boldsymbol{k_{eff}}$	Effective conductivity tensor	W/mK
$\boldsymbol{q_r}$	Involves all the thermal phenomena related to the radiative heat transfer	J
$\boldsymbol{q_c}$	Conductive term	W/m^2
p	Pressure	Pa
I	Intensity radiation	W/m^2
I_b	Intensity radiation of the black body	W/m^2
Ω	Direction of radiation	rad
Φ	Phase function	-
σ_s	Fractions of radiations attenuated or scattered	(0–1)
k_a	Absorption coefficient	(0–1)
β	Extinction coefficient	(0–1)
k_e	Emissivity coefficient	(0–1)
a_1	Probability of scattering in any direction	%
μ_0	Angle between the direction of the scattered radiation and the osculating plane	rad
$\boldsymbol{\tau}$	Viscous stress tensor	Pa
$\boldsymbol{S}$	Strain tensor	1/s
t	Time	s
ΔT	Temperature difference	K
a_n	Coefficients of the polynomial function	-
R^2	Square of the Pearson correlation coefficient	-
m	*Slope* of the least square line (in double ln scale)	Ln(K/s)

References

1. Bozsaky, D. The historical development of thermal insulation materials. *Architecture* **2010**, *41/2*, 49–56. [CrossRef]
2. Bynum, R.T. *Insulation Handbook*; The McGraw-Hill Companies: New York, NY, USA, 2001.
3. Morley, M. *Building with Structural Insulated Panels (SIPs): Strength and Energy Efficiency Through Structural Panel Construction*; The Taunton Press: Newtown, CO, USA, 2000.
4. Gil, L. Cork Composites: A Review. *Materials* **2009**, *2*, 776–789. [CrossRef]
5. Masri, Y.E.; Rakha, T. A scoping review of non-destructive testing (NDT) techniques in building performance diagnostic inspections. *Constr. Build. Mater.* **2020**, *265*, 120542. [CrossRef]
6. Malanho, S.; Veiga, R.; Farinha, C.B. Global performance of sustainable thermal insulating systems with cork for building facades. *Buildings* **2021**, *11*, 83. [CrossRef]
7. Lagorce-Tachon, A.; Mairesse, F.; Karbowiak, T.; Gougeon, R.D.; Bellat, J.-P.; Sliwa, T.; Simon, J.-M. Contribution of image processing for analyzing the cellular structure of cork. *J. Chemom.* **2018**, *32*, e2988. [CrossRef]
8. Liu, Y.; Cao, Z.; Wang, Y.; Wang, D.; Liu, J. Experimental study of hygro-thermal characteristics of novel cement-cork mortars. *Constr. Build. Mater.* **2021**, *271*, 121910. [CrossRef]
9. Merabti, S.; Kenai, S.; Belarbi, R.; Khatib, J. Thermo-mechanical and physical properties of waste granular cork composite with slag cement. *Constr. Build. Mater.* **2021**, *272*, 121923. [CrossRef]
10. Novais, R.M.; Senff, L.; Carvalheiras, J.; Lacasta, A.M.; Cantalapietra, I.R.; Labrincha, J.A. Simple and effective route to tailor the thermal, acoustic and hygrothermal properties of cork-containing waste derived inorganic polymer composites. *J. Build. Eng.* **2021**, *42*, 102501. [CrossRef]
11. Schabowicz, K. Non-destructive Testing of Materials in civil Engineering. *Materials* **2019**, *12*, 3237. [CrossRef] [PubMed]
12. Chizh, M.; Zhuravlev, A.; Razevig, V.; Ivashov, S.; Farloni, P.; Capineri, L. Defects investigation in thermal insulation coatings with microwave imaging based on a 22 GHz holographic radar. *NdtE Int.* **2020**, *109*, 102191. [CrossRef]
13. Aditya, L.; Mahlia, T.M.I.; Rismanchi, B.; Ng, H.M.; Hasan, M.H.; Metselaar, H.S.C.; Muraza, O.; Aditiya, H.B. A review on insulation materials for energy conservation in buildings. *Renew. Sustain. Energy Rev.* **2017**, *73*, 1352–1365. [CrossRef]
14. Meola, C. Infrared thermography of masonry structures. *Infrared Phys. Techn.* **2007**, *49*, 228–233. [CrossRef]
15. Barreira, E.; Almeida, R.M.S.F.; Delgado, J.M.P.Q. Infrared thermography for assessing moisture related phenomena in building components. *Constr. Build. Mater.* **2016**, *110*, 251–269. [CrossRef]

16. Aversa, P.; Palumbo, D.; Donatelli, A.; Galietti, U.; Tamborrino, R.; Luprano, V.A.M. Infrared thermography for the investigation of dynamic thermal behaviour of opaque building elements: Comparison between empty and filled with hemp fibres prototype walls. *Energ. Build.* **2017**, *152*, 264–272. [CrossRef]
17. Marani, R.; Palumbo, D.; Galietti, U.; Stella, E.; D'Orazio, T. Automatic detection of subsurface defects in composite materials using thermography and unsupervised machine learning. In Proceedings of the 2016 IEEE 8th International Conference on Intelligent Systems (IS), Sofia, Bulgaria, 4–6 September 2016. [CrossRef]
18. D'Accardi, E.; Palumbo, D.; Tamborrino, R.; Galietti, U. Quantitative analysis of thermographic data through different algorithms. *Procedia Struct. Integr.* **2018**, *8*, 354–367. [CrossRef]
19. Palumbo, D.; Cavallo, P.; Galietti, U. An investigation of the stepped thermography technique for defects evaluation in GFRP materials. *NdtE Int.* **2019**, *98*, 254–263. [CrossRef]
20. Sfarra, S.; Perilli, S.; Guerrini, F.; Bisegna, F.; Chen, T.; Ambrosini, D. On the use of phase change materials applied on cork-coconut-cork panels. A thermophysical point of view concerning the beneficial effect in terms of insulation properties. *J. Anal. Calorim.* **2018**, *132*, 4061–4090. [CrossRef]
21. Perilli, S.; Sfarra, S.; Guerrini, F.; Bisegna, F.; Ambrosini, D. The thermophysical behaviour of cork supports doped with an innovative thermal insulation and protective coating: A numerical analysis based on in situ experimental data. *Energ Build.* **2018**, *159*, 508–528. [CrossRef]
22. Fino, R.; Tadeu, A.; Simões, N. Influence of a period of wet weather on the heat transfer across a wall covered with uncoated medium density expanded cork. *Energ. Build.* **2018**, *165*, 118–131. [CrossRef]
23. Cherki, A.; Remy, B.; Khabbazi, A.; Jannot, Y.; Baillis, D. Experimental thermal properties characterization of insulating cork–gypsum composite. *Constr. Build. Mater.* **2014**, *54*, 202–209. [CrossRef]
24. Şen, A.; Bulcke, J.V.; Defoirdt, N.; Acker, J.V.; Pereira, H. Thermal behaviour of cork and cork components. *Thermochim. Acta* **2014**, *582*, 94–100. [CrossRef]
25. Badghaish, A.A.; Fleming, D.C. Fleming, Non-destructive inspection of composites using step heating thermography. *J. Compos. Mat.* **2008**, *42*, 1337–1357. [CrossRef]
26. Balageas, A.A.; Roche, J.M. Common tools for quantitative time-resolved pulse and step-heating thermography–part I: Theoretical basis. *Quant. IR J.* **2014**, *11*, 43–56. [CrossRef]
27. Jeager, J.; Carslaw, H. *Conduction of Heat in Solids*; Oxford University Press: London, UK, 1959.
28. Cengel, Y.A. *Introduction to Thermodynamics and Heat Transfer*; McGraw-Hill: New York, NY, USA, 1997.
29. Marani, R.; Palumbo, D.; Galietti, U.; D'Orazio, T. Deep learning for defect characterization in composite laminates inspected by step-heating thermography. *Opt. Laser Eng.* **2021**, *145*, 106679. [CrossRef]
30. Hamdami, N.; Monteau, J.-Y.; Le Bail, A. Effective thermal conductivity of a high porosity model food at above and sub-freezing temperatures. *Int. J. Refrig.* **2003**, *26*, 809–816. [CrossRef]
31. ASTM E1862-14. *Standard Practice for Measuring and Compensating for Reflected Temperature Using Infrared Imaging Radiometers*; ASTM International: West Conshohocken, PA, USA, 2018. Available online: www.astm.org (accessed on 21 April 2019).
32. ASTM E1933-14. *Standard Practice for Measuring and Compensating for Emissivity Using Infrared Imaging Radiometers*; ASTM International: West Conshohocken, PA, USA, 2018. Available online: www.astm.org (accessed on 21 April 2019).
33. Available online: www.tecnosugheri.it/prodotto/corkpan/ (accessed on 3 May 2019).
34. Barreira, E.; Bauer, E.; Mustelier, N.; de Freitas, V.P. Measurement of materials emissivity—Influence of the procedure. In Proceedings of the AITA—13th International Workshop on advanced Infrared Technology & Applications, Pisa, Italy, 29 September–2 October 2015; pp. 242–245.
35. Paulescu, M.; Paulescu, E.; Gravila, P.; Badescu, V. *Weather Modeling and Forecasting of PV Systems Operation*; Green Energy and Technology; Springer: London, UK, 2013.
36. Sfarra, S.; Ibarra-Castanedo, C.; Theodorakeas, P.; Avdelidis, N.P.; Perilli, S.; Zhang, H.; Nardi, I.; Koui, M.; Maldague, X.P.V. Evaluation of the state of conservation of mosaics: Simulations and thermographic signal processing. *Int. J. Sci.* **2017**, *117*, 287–315. [CrossRef]
37. Available online: www.indemar.com/s/Shield-Coat-250-Scheda-tecnica-INDEMAR.pdf (accessed on 3 May 2019).
38. Vires Srl Website. Available online: www.vires.it (accessed on 20 April 2017).
39. Sieger, R.; Howell, J. *Thermal Radiation Heat Transfer*, 4th ed.; Taylor & Francis: New York, NY, USA, 2002.
40. Incropera, F.P.; DeWitt, D.P. *Fundamentals of Heat and Mass Transfer*, 5th ed.; John Wiley & Sons: Hoboken, NJ, USA, 2002.
41. Modest, M.F. *Radiative Heat Transfer*, 2nd ed.; Academic Press: San Diego, CA, USA, 2003.
42. Fiveland, W.A. The Selection of Discrete Ordinate Quadrature Sets for Anisotropic Scattering. *Fundam. Radiat. Transf.* **1991**, *160*, 89–96.
43. Palumbo, D.; Galietti, U. Damage investigation in composite materials by means of new thermal data processing procedures. *Strain* **2016**, *52*, 276–286. [CrossRef]
44. Shepard, S.M. Advances in pulsed thermography. *Proc. SPIE* **2001**, *511*, 4360. [CrossRef]
45. Ahi, K. A method and system for enhancing the resolution of terahertz imaging. *Measurement* **2019**, *138*, 614–619. [CrossRef]
46. Ahi, K.; Jessurun, N.; Hosseini, M.-P.; Asadizanjani, N. Survey of terahertz photonics and biophotonics. *Opt Eng* **2020**, *59*, 061629. [CrossRef]